Applied Thermal Engineering 179 (2020) 115689

Contents lists available at ScienceDirect

Applied Thermal Engineering

journal homepage: www.elsevier.com/locate/apthermeng

Experimental assessment of the fluid charge distribution in an organic Rankine cycle (ORC) power system

Rémi Dickes*, Olivier Dumont, Vincent Lemort

Thermodynamics Laboratory, Faculty of Applied Sciences, University of Liège, Allée de la Découverte 17, B4000 Liège, Belgium

HIGHLIGHTS

- Load cells and an infrared camera are used to assess the fluid distribution in an ORC unit.
- An extensive experimental campaign including 330 steady-state points is conducted.
- Fluid distribution and temperature profiles in the heat exchangers are directly correlated.
- The evaporator charge requirement dictates the condenser and the liquid receiver operation.
- The ORC charge and the receiver size are key parameters to optimize the system performance.

ARTICLE INFO

Keywords:
Charge
Measurement
ORC
Fluid distribution
Infrared
Experiments

ABSTRACT

This paper reports on experiments aiming to understand and to characterize how the working fluid spreads in an organic Rankine cycle (ORC) power system. To this end, a 2-kW_e ORC test rig is constructed and tested over a wide range of conditions. Besides standard thermo-hydraulic sensors, the fluid charge distribution is measured on-line by bending load cells and infrared imaging techniques. Following a complete experimental campaign (which includes more than 330 steady-state points and fully characterizes the ORC off-design behaviour), a dual data reconciliation method is applied to the raw measurements to obtain a reference dataset. The results are then analysed to assess the charge distribution mechanisms occurring in the ORC and how it is correlated with the system performance. Among other aspects, this paper demonstrates (i) how the charge inventory is highly correlated to the temperature profiles in the heat exchangers, (ii) how the evaporator dictates the operating conditions of the low-pressure components, and (iii) how the system charge and the liquid receiver size can be selected to maximize the ORC overall performance.

1. Introduction

Because they are specifically suited for small-capacity and low-grade heat sources, a common aspect of organic Rankine cycle (ORC) systems is the versatile nature of their operating conditions [1]. Whether for solar, geothermal or waste heat recovery applications, their boundary conditions (i.e. the heat source, the heat sink, and eventually the expander load) often deviate from design expectations, imposing ORC units to adapt their working regime for performance or safety reasons. Such operating conditions are referred to as *off-design* (i.e. they differ from the nominal design point) and ordinarily result in a performance deterioration. Either for system-level integration, on-site performance optimization or control development, a proper prediction of the ORC off-design behaviour is mandatory and reliable models are needed. In order to develop a *true* off-design model[1], both fundamental principles of thermodynamics must be accounted for, namely the conservation of energy and the conservation of mass. Besides modelling the energy transfers, a true off-design model must account for the constant amount of working fluid (known as the *charge*) enclosed in the system and for its distribution among the components as a function of the operating conditions. Such a consideration is referred to as *charge-sensitive*.

Charge-sensitive modelling is an innovative field of research for ORC systems and a few papers have been published since 2015. As reported in

* Corresponding author.
E-mail addresses: rdickes@ulg.ac.be (R. Dickes), olivier.dumont@ulg.ac.be (O. Dumont), vincent.lemort@ulg.ac.be (V. Lemort).

[1] By "true off-design model", the authors refer to a simulation tool able to predict the performance of an ORC unit solely based on its components specifications and its boundary conditions, i.e. without making any assumption on the working fluid inner state (like an imposed subcooling). For more details on this issue, please refer to the authors' previous publications [2,3].

https://doi.org/10.1016/j.applthermaleng.2020.115689
Received 13 August 2019; Received in revised form 20 May 2020; Accepted 30 June 2020
Available online 04 July 2020
1359-4311/

Nomenclature

Acronyms

AC	Air Conditioning
AUX	Auxiliary
BPHEX	Brazed Plate Heat Exchanger
CD	Condenser
CHP	Combined Heat and Power
EV	Evaporator
EVM	Expanded Vapour Measurement
EXP	Expander
FCHEX	Fin Coil Heat Exchanger
FS	Full Scale
HEX	Heat Exchanger
HP	Heat Pump
HT	High Temperature
HTF	Heat Transfer Fluid
HVAC	Heating, Ventilation, Air Conditioning
IR	Infrared
LC	Load Cell
LR	Liquid Receiver
LT	Low Temperature
MT	Medium Temperature
OLM	On-Line Measurement
ORC	Organic Rankine Cycle
POE	Polyolester
PP	Pump
QCV	Quick Closing Valve
REC	Recuperator
RW	Remove-and-Weigh
VFD	Variable Frequency Drive
WF	Working Fluid
WHR	Waste Heat Recovery

Subscripts

amb	ambient
c	cold
cd	condensing
ev	evaporating
ex	exhaust
exp	expander
h	hot
htf	heat transfer fluid
i,j	index
liq	liquid
m	mean
pp	pump
sat	saturation
sc	subcooling
sh	superheating
su	supply
tot	total
vap	vapour
wf	working fluid

Variables

α	Void Fraction, (–)
Δ	Difference, (–)
η	Efficiency, (–)
ρ	Density, (kg/m^3)
σ	Sensor Accuracy, (–)
θ	Pinch, (K)
A	Area, (m^2)
c	Corrected value, (–)
e	Voltage, (V)
g	gravity constant, (m/s^2)
H	Height, (m)
M	Mass, (kg)
$\dot{m}$	Mass flow rate, (kg/s)
P	Pressure, (bar)
$\dot{Q}$	Heat flow rate, (W)
s	Entropy, (J/kg.K)
T	Temperature, (°C)
U	Heat transfer coefficient, (W/m^2.K)
$\dot{V}$	Volume flow rate, (m^3/s)
$\dot{W}$	Power, (W)
x	Quality, (–)
$\mathbf{f}/\mathbf{g}$	Mathematical functions, (–)

Table 1, however, none of these models have been fully validated. Existing works either exploited unvalidated simulation tools (e.g. [7,9]), or the proposed validation was incomplete (e.g. [3,6,8]). At best, the model reliability was assessed by comparing its thermodynamic predictions (i.e. temperatures, pressures, mass flows and energy transfers) to experimental data while imposing the total charge of the system as input. Although necessary, such a comparison is not sufficient. To completely validate a charge-sensitive model, its charge inventory predictions must also be verified. One must ensure that the fluid repartition simulated numerically corresponds to the reality. However, an intrinsic monitoring of the working fluid distribution among the ORC components has not yet been conducted. Until now, such charge-oriented measurements have been limited to HVAC systems only. For instance, Table 2 summarizes a non-exhaustive list of investigations conducted on heat pumps or air-conditioning systems. As shown in the last column, most of these studies employed *quick-closing valve* (QCV) approaches to assess the working fluid distribution [19]. With these methods, the system is divided into different sections with actuated valves. Under normal operation, the valves are left open so the working fluid can circulate freely in the system. Once the mass measurement is desired, all the valves are shut simultaneously so as to trap the refrigerant in the various control volumes. From then, various techniques have been elaborated on to estimate the charge enclosed in the different sections. Although “brutals”, such QCV methods can provide highly accurate results if they are properly executed (down to the gram scale). However, they require stopping and discharging the system for every single mass measurement, which is extremely time-consuming and can lead to leakage issues. In opposition to QCV methods, *on-line measurement* (OLM) techniques allow a continuous recording of the fluid mass repartition without interfering with the system operation. To this end, force transducers (e.g. a load cell or a scale) are installed on some mechanical apparatus in order to detect variations of mass within specific components. Despite offering a lower accuracy and requiring some sensors calibrations, this approach is not intrusive and is much faster. To this date, none of these techniques have ever been applied to an ORC power unit. Any experimental quantification of the charge distribution in an organic Rankine cycle is still missing, which prevents a complete validation of charge-sensitive models. The proposed work aims to fill this lack of knowledge. More specifically, the objective of this paper is twofold:

(i) to present an innovative methodology and experimental apparatus for recording the fluid distribution in a small-scale ORC system;
(ii) to present the results of an extensive experimental campaign from which the charge distribution mechanisms are assessed.

The paper is organized as follows: first, the test rig used as case

Table 1
Charge-sensitive modelling studies applied to ORC systems.

Authors	System description	Summary
Yousefzadeh et al. (2015) [4]	10-kW_e ORC prototype (non-recuperative, WF = R134a, screw expander, shell-and-tube HEX, liquid receiver)	Development of a mass-conserving dynamic model. Finite-volume method for HEX simulation. Steady-state validation with experimental data (without verifying charge inventory predictions). Off-design simulations to analyse the ORC response and the charge migration under transient operations.
Desideri (2016) [5]	11-kW_e ORC unit (R245fa, BPHEXs, screw expander, centrifugal pump)	Dynamic modelling of ORC systems in Dymola. Comparison of finite-volume and moving -boundary methods for HEX modelling. Steady-state and dynamic validation of the model thermodynamic predictions (no validation regarding the charge inventory predictions).
Ziviani et al. (2016) [6]	Two experimental systems: (i) 11-kW_e ORC unit (R245fa, BPHEXs, screw expander, centrifugal pump); (ii) 5-kW_e ORC unit (R134a, BPHEXs, scroll expander, diaphragm pump)	Steady-state modelling. Development and validation of a steady-state model that is either charge-sensitive or subcooling-sensitive. The ORC model and the subcomponent models are validated with experimental measurements (no validation regarding the charge inventory predictions).
Dickes et al. (2017) [3]	Experimental 2-kW_e ORC unit for solar application (WF = R245fa, scroll expander, BPHEXs, air-cooled condenser, diaphragm pump.)	Development of a steady-state charge-sensitive model for entire ORC system. Use data on the charge for identifying the convective heat transfer coefficients. Experimental data comparison for thermodynamic and global charge validations.
Liu et al. (2017) [7]	Theoretical 3-kW_e WHR ORC system (WF = R123, scroll expander, shell-and-tube condenser, fin-tube evaporator, no recuperator)	Development of a charge-sensitive model used to (i) compute the charge of WF in nominal conditions; (ii) study the heat exchangers behaviour in part-load conditions; (iii) assess the impact of different charges in part-load conditions.
Santos et al. (2018) [8]	Experimental micro-CHP 1.5-kW_e/35-kW_{th} ORC (WF = R245fa, scroll expander, rotary vane pump, gas burner, no recuperator)	Development of a charge-sensitive modular modelling library implemented in Fortran. Combination of empirical and semi-empirical models to study the whole system. Charge computation in HEX is unclear regarding the density calculation. Thermodynamic validation with experimental data. No comparison with charge measurements.

Table 2
Non-exhaustive review of experiments evaluating the charge distribution in HVAC systems (QCV = quick-closing-valve, OLM = on-line measurement, RW = remove-and-weigh, EVM = expanded-vapour-measurement).

Authors (year)	System (capacity)	Fluid (charge)	Method
Tanaka et al. (1982) [10]	Household HP (3.5-kW_h)	R22 (950 g)	QCV + RW
Mulroy et al. (1983) [11]	Household AC (10-kW_c)	R22 (4 kg)	QCV + RW
Miller et al. (1985) [12]	Household HP (10-kW_h)	R22 (5.7 kg)	OLM
Belth et al. (1988) [13]	Household HP (10-kW_h)	R22	OLM
Grodent (1998) [14]	Household AC (8-kW_c)	R22 (1.7–2.4 kg)	OLM
Primal et al. (2001) [15]	Household HP (5-kW_h)	R290	QCV + RW
Hoehne et al. (2004) [16]	Prototype (1.5-kW_c)	R290 (150 g)	QCV + RW
Bjork et al. (2006) [17,18]	Domestic refrigerator (0.1-kW_c)	R600a (34 g)	QCV + EVM
Ding et al. (2009) [19]	Household AC (7.1-kW_c)	R410A (2 kg)	QCV + RW
Peuker (2010) [20]	Automotive AC (4-kW_c)	R134a (1 kg)	QCV + RW
Wujek et al. (2014) [21]	Household AC/HP (10-kW_c)	R410A/R32	QCV + RW
Li et al. (2015) [22]	Household AC (2.6-kW_c)	R290 (250–350 g)	QCV + RW
Tang et al. (2017) [23]	Household AC	R290 (260–350 g)	QCV + RW
Li et al. (2018) [24]	Household AC (2.6-kW_c)	R410A (1.06 kg)	QCV + RW

study is presented in Section 2. Then, in Section 3, a complete description of the methodology is provided (including the various means of measurement, the experimental campaign and the raw data post-treatment method). Finally, from the experimental data, mechanisms dictating the fluid distribution and its impact on the ORC performance are discussed in Section 4.

This article summarizes the experimental investigations conducted in Dickes's PhD thesis [25]. For any further detail on the results or the methodology, one is invited to consult the original manuscript.

2. Case study

The case study considered in this work is a 2-kW_e ORC unit developed and constructed at the University of Liége [26,27]. Depicted in Fig. 1, the system features a conventional recuperative architecture and employs R245fa as working fluid. Both the evaporator and the recuperator are brazed plate heat exchangers while an air-cooled fin coil heat exchanger is used for the condenser. The system includes a liquid receiver at the condenser outlet and a filter/dryer in the pump exhaust line. The working fluid is pressurized with a multi-diaphragm pump and is expanded through a lubricated scroll expander for power generation. In order to limit heat transfers with the ambient, all the components and the pipelines are thermally insulated. In terms of control, speeds of the pump and the condenser fan are both regulated with variable-frequency drives while the expander is indirectly controlled by adjusting its electrical load. In order to permit a complete monitoring of the system performance, the test rig is instrumented with a large set of sensors. As shown in Fig. 1, standard T-type thermocouples, flow meters, pressure transducers and power meters are placed at every key location of the unit. For further information, a complete summary of the ORC characteristics and photos of the system are provided in Appendix A. Finally, it is worth emphasizing that the proposed case study is not a particular prototype, but a rather common technology for micro- to medium-scale power applications. Numerous ORC units featuring the same type of working fluid, components and system architecture have been built for both research [28–30] and commercial purposes (e.g. the Power + units from ElectraTherm® [31] or the LT/MT/HT-series from Rank® [32]).

3. Methodology

Taking the above test rig as case study, the following approach is

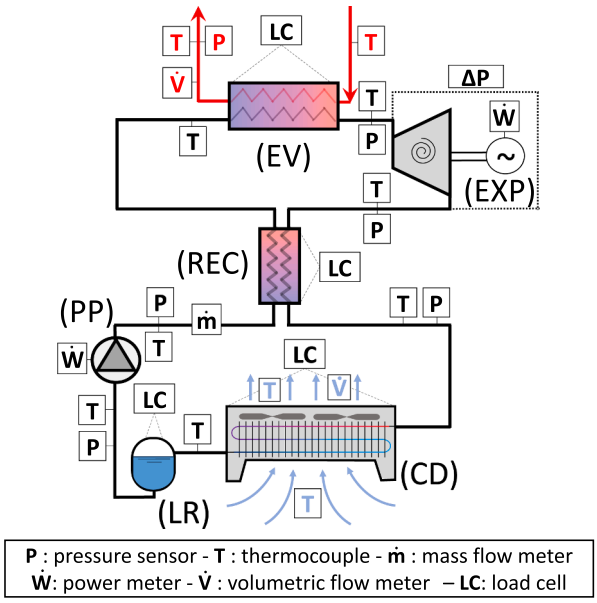

Fig. 1. Layout and sensors location of the 2-kW$_e$ ORC system.

employed to assess its charge inventory as a function of the operating conditions.

3.1. On-line charge monitoring

Besides standard thermo-hydraulic sensors, the test rig allows a direct monitoring of the fluid distribution among the ORC components. Because of the little contribution of the machinery in the charge inventory (i.e. the mass enclosed in the pump and the expander is negligible [2]), only the three exchangers and the liquid receiver are recorded using an on-line measurement technique. More specifically, each of these four components is suspended and weighted by a bending load cell as depicted in Fig. 2. Dedicated clamping structures are thus designed to position and to hang the components within the test rig. Once properly placed, the elements are connected to the ORC circuit using flexible anti-vibration hoses. In order to mechanically isolate the suspended components from the rest of the system (and to least interfere with the load cells measurements), the extremity of each flexible hose is firmly held to the test bench structure with holding clamps. For instance, the apparatus constructed for weighting the recuperator is depicted in Fig. 3 (photos of the other components are provided in Appendix A). Following this approach, the load cells cannot be employed as absolute mass sensors, but rather as detectors of mass variations. Besides mechanical disturbances induced by the interconnecting pipes, the system operating conditions (i.e. the fluid pressure and temperature) also interfere with the apparent weight seen by the force transducers. In order to account for these perturbations, and to properly correlate the sensors signals with the actual charge enclosed in the components, a dedicated calibration is conducted for each load cell individually. More specifically, reference weights are attached under each of the four components and their load cells signals are recorded while varying:

- the pressure inside the pipes (by injecting nitrogen in the test bench);

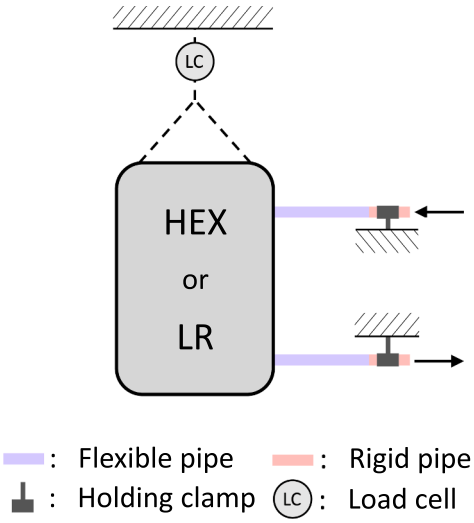

Fig. 2. Scheme of the on-line charge measurement method.

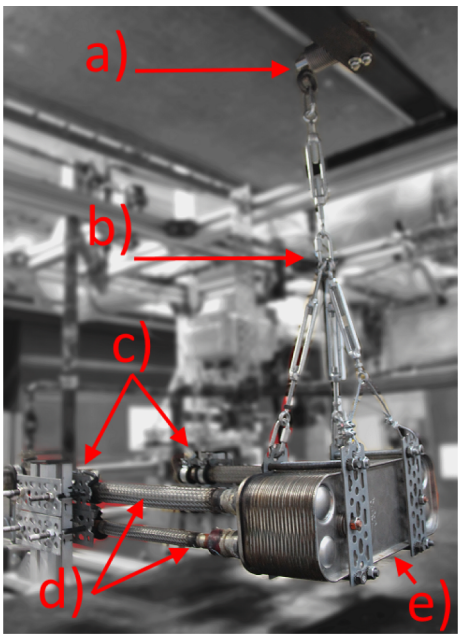

Fig. 3. Mechanical apparatus to record the charge in the recuperator (a) load cell (b) hanging structure (c) holding clamps (d) flexible hoses (e) recuperator.

- the temperature of the pipes (by using a heat gun and hot thermal oil coming from the electrical boiler)[3].

For instance, the results obtained when calibrating the liquid receiver are given in Fig. 4. As seen, the operating pressure has a shifting impact on the signals-charge relationship which must be taken into account. Similarly, a complete cartography of each load cell response is constructed. By using these calibration data, triangulation-based interpolants are fitted to retrieve the actual mass enclosed in each component from the sensors signals and the local operating conditions. Ultimately, the charges M_i are monitored i.e.

$$M_i = \mathbf{f_i}(e_i, T_{ij}, P_{ij}) \quad (1)$$

where $\mathbf{f_i}$ are the fitted interpolatant, e_i are the load cells output voltage

[2] Although the pump encloses a high-density fluid (i.e. a liquid phase), its inner volume is limited (<20 cc). Combining both effects, its charge enclosure is negligible (<30 g) in comparison to the heat exchangers or the liquid receiver (enclosing several kilograms of fluid). The same conclusion is true for the expander, but for the opposite reasons: the expander volume is much bigger, but it encloses a vapour phase (low density), resulting too in a negligible charge.

[3] The impact of the temperature appeared to be significant for conditions exceeding 120°C, i.e. for the evaporator only. For further details on this aspect, please refer to the original manuscript [25].

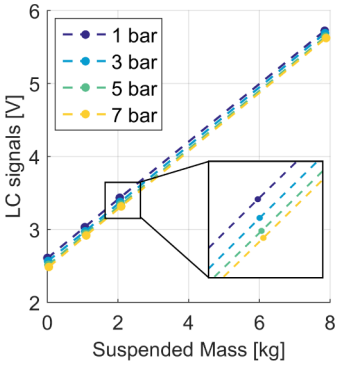

Fig. 4. Suspended mass vs. LC output at different operating pressures (case of the liquid receiver).

and T_{ij} (resp. P_{ij}) are the supply and discharge temperatures (resp. pressures) measurements.

A key advantage of the above method is its non-intrusive nature. Unlike quick-closing-valve approaches, the proposed on-line technique allows the charge distribution to be recorded without interfering with the system operation. A wide range of conditions can thus be investigated in a minimal amount of time and a direct monitoring of the fluid migration under transient regimes is also possible (see Section 5 for an example). On the other hand, this on-line method features a relatively limited accuracy. As the whole components have to be hung to the load cells, large-scale force transducers (up to 250 kg for the condenser) are needed to detect small amounts of fluid. Accounting for the uncertainty propagation of all the sensors, the total charge recorded in the ORC system is estimated within a ±2 kg accuracy (see Table A.6 for the accuracy of each component individually). The proposed method thus suitably characterizes how the fluid spreads at a system-level, but it does not perfectly monitor the charge enclosed in a specific component.

3.2. Infrared imaging of the condenser

As further discussed in Section 4, the charge distribution in an ORC system is highly correlated with the temperature profiles in the heat exchangers. In order to best identify how the fluid is spread in the present case study (i.e. among the components, but also within them), the condenser permits an additional investigation [33]. The condenser is a fin coil heat exchanger in which parallel tubes each effectuate 12 passes in a matrix of plain fins. While the tubes are mostly invisible from the outside, their extremity can be observed if the condenser casing is removed. By using an infrared camera, as depicted in Fig. 5, the temperature evolution along these channels can be recorded at 13 discrete positions. Although the temperature profile is not continuously monitored, these infrared (IR) data help to more precisely localize the spatial frontiers between the liquid, the vapour and the two-phase zones. In this work, a set of 4 IR photos is taken with a Flir E50 camera to study every operating condition tested experimentally. Each photo is shot from a specific point of view (two at the front, two at the back) in order to fully monitor the condenser temperature profile. For instance, the photos collected for one operating point are given in Fig. 6. The IR photos #1 and #4 offer an overview of the temperature distribution in the complete tubes bank, while photos #2 and #3 focus on a specific channel. After verifying that the temperature distribution in the heat exchanger is quasi-homogeneous (i.e. that there are no significant discrepancies between the different channels), the temperature profile along one typical path is extracted. To this end, a semi-automated algorithm is run to quickly locate the end-tips of this particular channel on the different photos (i.e. the red crosses in Fig. 6). The temperatures are then retrieved from the IR data corresponding to the selected pixels. In order to avoid any viewing angle effect [34], the pixel locations are

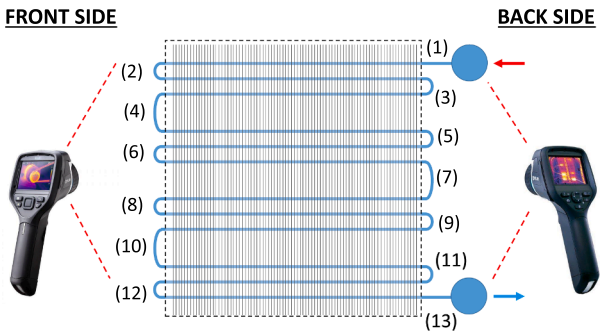

Fig. 5. Configuration and position numbering for one channel in the condenser.

selected so the tube's outer surface is always normal to the IR camera. A post-treatment algorithm is then applied to merge the temperature profiles identified on the front side (i.e. from photo #2) and the back side (i.e. from photos #3 and #4) of the condenser. Because the tube emissivity is not perfectly known and because the photos are not taken from the same distance, the two temperature profiles cannot be simply superposed. Indeed, each photo gives an image of the relative temperature gradient seen from a specific point of view, but they do not share the same absolute reference. To overcome this issue, the temperatures profiles are shifted and combined so as to comply with the saturation temperatures gathered by the pressure sensors. More specifically, the merging algorithm relies on two main steps, i.e.

- to identify the pseudo-isothermal region in which the condensation process occurs on both the front and back sides;
- to merge the front and the back temperature profiles assuming a continuity in the two-phase region.

The temperature profile identified for the above example is depicted in Fig. 7 and highlights how the zones' spatial distribution can be estimated. This infrared imaging method is applied for every point tested with the ORC unit. Although theoretically feasible (e.g. see [35,36]), such IR monitoring is not conducted for the two plate heat exchangers (i.e. the recuperator and the evaporator) as it would require the removal of their thermal insulation and thus yield undesired heat losses.

3.3. Experimental campaign

To fully investigate the system behaviour, an experimental campaign accounting for more than 300 operating hours is conducted with the test rig. Ultimately, a set of 330 steady-state points is gathered to characterize the ORC operation. Those steady-state points are obtained by averaging the raw dynamic measurements over 10-min periods in stabilized conditions[4]. Such a long time window is chosen to minimize the impact of the noise disrupting the load cells signals. The tests are performed without following any dedicated control strategy, but rather to induce significant fluid migration through the components. The system is thus operated over extended ranges of conditions, including non-optimal performance points. To this end, *all* the system boundary conditions are varied, including the total charge of working fluid enclosed in the ORC unit. Ultimately, six different charges of working fluid are tested (14.3 kg, 16.6 kg, 19.6 kg, 25 kg, 28 kg and 31.2 kg). Boundaries of the experimental campaign are summarized in Table 3. Complete details regarding the database can be found in Appendix B.

[4] Conditions are considered as stabilized when deviations in all the temperatures are lower than 1°C, pressures are non-sliding and relative deviations for all mass flow rates remain lower than 1%.

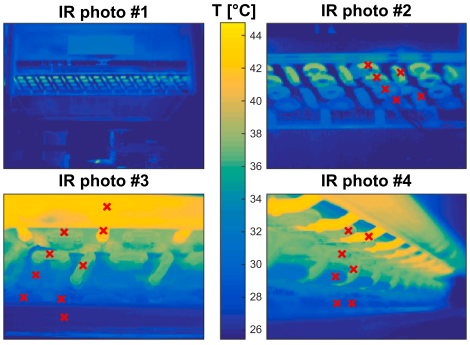

Fig. 6. Example of IR photos for one operational point.

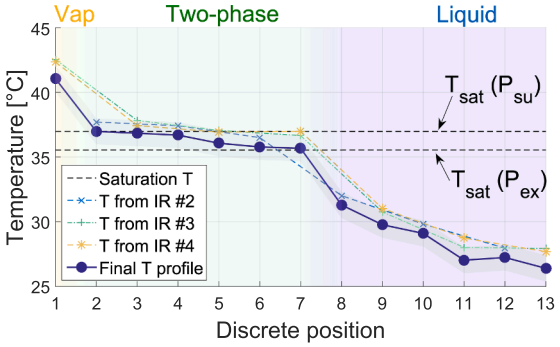

Fig. 7. Temperature profile of the example presented in Fig. 6.

Table 3
Boundaries of the experimental database.

Variable	Min.	Max.	Unit
Heat source flow rate	0.05	1.1	l/s
Heat source supply temperature	66	150	°C
Heat sink flow rate	0.2	1.2	m^3/s
Heat sink supply temperature	13	27	°C
Evaporating pressure	3.9	15.2	bar
Condensing pressure	1.2	6.1	bar
Expander rotational speed	1900	7300	RPM
Pump rotational speed	160	1080	RPM
WF mass mass flow rate	23	155	g/s
Expander power output	108	1875	W
Net ORC efficiency ($= (\dot{W}_{exp} - \dot{W}_{pp} - \dot{W}_{cd})/\dot{Q}_{ev}$)	−2.7	6	%
Charge of working fluid	14.3	31.2	kg
Charge of lubricant	1.5	1.5	kg

3.4. Data reconciliation

The raw measurements gathered experimentally provide valuable insights into the ORC operation but they do not constitute a perfect image of the reality. As reported in Table A.6, all the sensors employed to monitor the test rig have a limited accuracy. While the error committed by each individual sensor remains limited locally, the propagation of these uncertainties when assessing the global system performance can lead to significant inaccuracies. In order to improve the dataset quality, a reconciliation method is applied. Data reconciliation is a mathematical tool aiming to retrieve the most probable state of a system out of experimental measurements while accounting for the sensors accuracies. More specifically, it identifies the smallest corrections to apply to the original measurements so that the system operation respects a set of constraints. Mathematically, it can be formulated as the constrained minimization of a penalty function $\mathbf{g}(c_i)$ i.e.

$$\min_{c_i} \mathbf{g}(c_i) = \sum_{i=1}^{N} \left(\frac{m_i - c_i}{\sigma_i} \right)^2 \quad (2)$$

where m_i are the original measurements, c_i are the corrected values and σ_i are the sensors standard deviations. In this work, both a *thermo-hydraulic* and a *charge inventory* reconciliation are conducted. More specifically, the raw database is reconciled so the ORC operation respects the following set of constraints, i.e. to verify

- valid heat balances in all three heat exchangers (Eqs. (B.1)–(B.3);
- direct redundancies between pressure sensors placed in series (Eqs. (B.4)–(B.7);
- a saturated liquid state at the condenser outlet if the liquid receiver is partially filled (Eq. B.8);
- positive pressure drops in the system (Eqs. B.9 and B.10);
- positive pinch points in the heat exchangers (Eqs. (B.11)–(B.13);
- a valid charge inventory in the whole system (Eqs. B.14).

Constitutive equations of these constraints are provided in Appendix B. Such a dual data reconciliation is applied for every operational point investigated experimentally. In order to ensure the viability of the reconciliation results, the difference between the reconciled values and the original measurements is checked to be within the sensors accuracies. Steady-state points that do not respect this condition, or those for which the optimization failed to respect the above constraints, are discarded (2 points in total). These *reconciled* measurements are now used as reference dataset in the next discussions.

4. Results and discussions

For the sake of conciseness, the analysis of the measurements is limited to aspects dealing with the charge distribution. More specifically, the experimental data is analysed to understand how the working fluid is spread in the ORC system and how it is correlated with the system operation.

4.1. Charge inventory and fluid phases occupation

Looking at the charge inventories monitored experimentally (see Fig. 8), the fluid distribution appears to be not uniform and - most importantly - to vary with the operating conditions. As highlighted in Eq. (3), the charge enclosed in every part of the system is dictated by two parameters only: the sections volume (V_i) and the fluid mean density within them ($\bar{\rho}_i$).

$$M_i = V_i \cdot \bar{\rho}_i \quad (3)$$

As the components volumes remain unchanged during operation, variations in the charge inventory are solely related with the fluid mean density. For all components, the fluid mean density can be expressed as

$$\bar{\rho}_i = (1 - \alpha_i)\rho_{liq,i} + \alpha_i \rho_{vap,i} \quad (4)$$

where $\rho_{liq,i}/\rho_{vap,i}$ are the liquid/vapour phases densities and α_i is the volume fraction occupied by the vapour phase ($\alpha_i = V_{vap,i}/V_i$, also known as *void fraction*). Charge modifications observed in Fig. 8 are not due to important variations of the single-phase densities (i.e. $\rho_{liq,i}/\rho_{vap,i}$), but rather to spatial redistributions of the liquid and vapour phases among the components (i.e. changes of α_i). Indeed, the components that always enclose single-phase flows present relatively stable charges whatever the operating conditions. For instance, the recuperator (which has mostly pure liquid and vapour flows on its cold and hot side, respectively) has a charge ranging continuously between 1.6 and 2 kg. Similarly, the charge enclosed in all the pipes, the pump and the expander remains close to 1.15–1.25 kg in all cases. On the other hand, the components that enclose both a liquid and a vapour phases (namely the evaporator, the condenser and the liquid receiver) evidence significant mass transfers.

About the liquid receiver, modifications of its inner charge are directly linked to its level of liquid. As illustrated in Fig. 9, the larger the liquid phase occupation, the higher the enclosed charge. Similarly, the

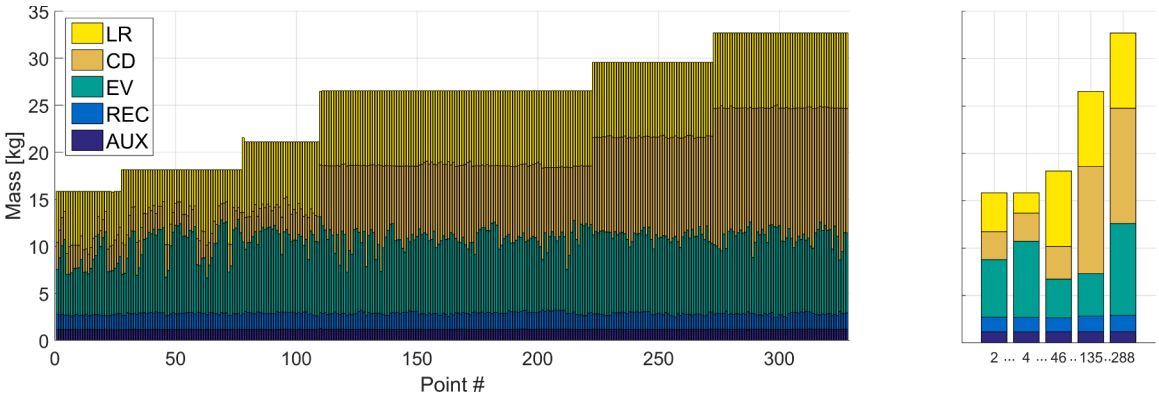

(a) Global results. (b) Zoom on 5 random points.

Fig. 8. Reconciled charge inventories recorded experimentally across the ORC (the AUX fraction includes the contributions of all the pipelines, the pump and the expander).

charge enclosed in the heat exchangers is directly bounded to the spatial occupation of the different phases and, by extension, to their temperature profiles. The ORC charge inventory is thus dependent on the subcooling and superheating levels observed at the inlet and outlet ports of the heat exchangers, but not exclusively. Another important parameter to take into account is the proximity of temperature profiles between the hot and cold media. As evidenced with a basic heat transfer equation, the mean temperature difference between the two fluids (ΔT_m) highly dictates the surface area (A) required to transfer a given amount of heat ($\dot{Q}$), i.e.

$$A = \frac{\dot{Q}}{U \Delta T_m} \tag{5}$$

where U is the effective heat transfer coefficient. Therefore, the pinch point location and its amplitude also play a crucial role in the zones spatial distribution, as well as in the system charge inventory. Such a situation is clearly illustrated in Fig. 10 with two points from the database. For both scenarios, the same amount of working fluid is present in the ORC (25 kg in total) and the liquid receiver is completely flooded (i.e. its mass is almost unchanged). However, the fluid repartitions between the condenser and the evaporator are notably different. In the first case, the evaporator presents a significant superheating at the outlet, and the pinch point (located at the hot port) is very narrow. A large fraction of the evaporator is thus filled by vapour and its charge is relatively low (17% of the total mass). Most of the fluid is consequently found in the condenser which encloses an important liquid zone. The large volume occupied by the liquid is not only related with the significant fluid subcooling observed at the outlet ($11K$), but also with the narrow pinch point located at the condenser cold port. In the second case, changes in the system operation (i.e. a decrease in both pump and expander speeds) induce a significant fluid transfer from the condenser to the evaporator. The evaporator now shows a smaller outlet superheating and the pinch point location is moved to the saturated liquid corner. A larger fraction of the evaporator is thus filled by liquid and its mass enclosure is more than doubled (now 36% of the total mass). The charge in the condenser is consequently diminished as it becomes less filled by liquid. As a direct consequence, the pinch point of the condenser is now located at the saturated vapour corner and the fluid outlet subcooling decreases to $4K$.

This example shows how the ORC charge distribution is bounded to the temperature profiles in the heat exchangers. Any operational parameter affecting these temperature profiles thus impacts the system charge inventory (cfr. Section 4.4). However, the total mass of fluid in the ORC remains constant in all cases. This charge conservation implies an operational dependency between the different components. If, for any reason, some fluid is withdrawn from one component, it must be transferred to another which thus alters its operating conditions.

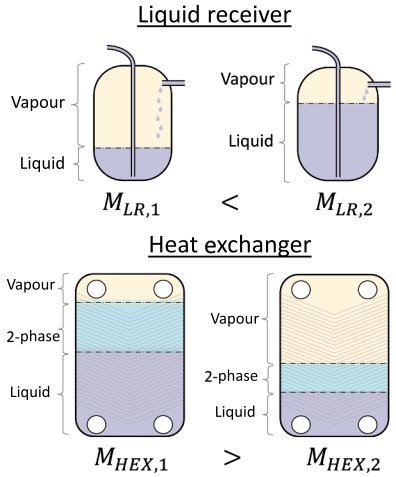

Fig. 9. Examples of phase distribution and its impact on the charge enclosure.

4.2. Charge-induced interdependency

A good mean to analyse such a charge-induced interdependency is to observe the ORC response when only the system charge is modified. To this end, six other points from the database are considered. More specifically, Fig. 11 depicts how the test rig evolves when the charge is increased while keeping all the other boundary conditions as constant as possible. At the lowest charge ($M1$), the liquid receiver is little filled and there is no liquid zone in the condenser. Most of the fluid is thus found in the evaporator, the liquid-phase pipelines and the cold-side recuperator. If the charge is raised ($M2$, $M3$), the liquid receiver plays a role of mass damper and, apart from the liquid level in the reservoir, nothing is much changed in the ORC operation[5]. When the charge exceeds 20 kg, the reservoir becomes completely flooded by liquid and it cannot absorb any more working fluid. From this point ($M4$ to $M6$), any

[5] In theory, *nothing* should change in the ORC operation as long as the liquid receiver is not completely flooded. In practice, however, all the boundary conditions could not be kept perfectly stable during the experiments - especially the ambient temperature varying between 22 to 26 °C - which slightly influences the experimental data depicted in Fig. 11. To better illustrate the sole impact of the charge, simulated predictions - gathered with a validated charge-sensitive model in which the ambient temperature was imposed at 23 °C - are also reported in dashed lines. For further detail regarding this modelling tool, please refer to Dickes's PhD manuscript [25].

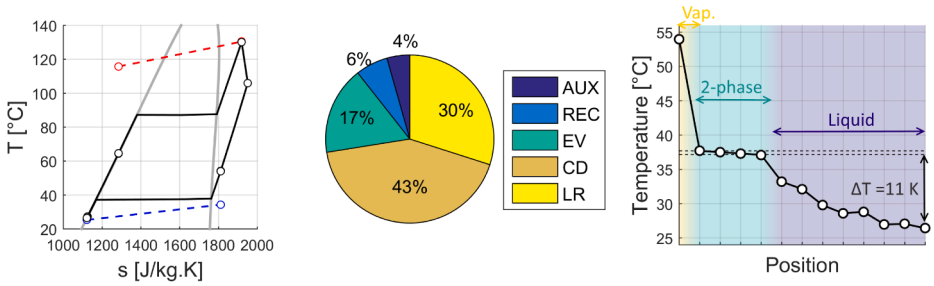

(a) Case 1: Low charge in the evaporator, high charge in the condenser (point #26 in database).

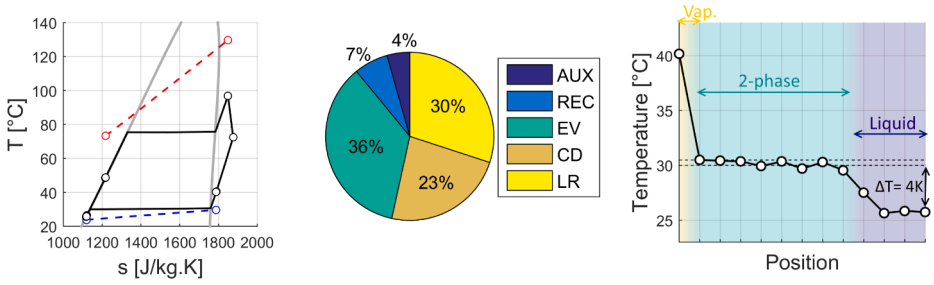

(b) Case 2: High charge in the evaporator, low charge in the condenser (point #30 in database).

Fig. 10. Impact of the temperature profiles on the charge distribution. Comparison of two scenarios in terms of T-s diagrams (left), charge distribution (middle) and IR profiles recorded in the condenser (right).

additional charge must be spread among the other components. However, the fluid distribution is not uniform. Almost all the charge is absorbed by the condenser, while the evaporator's contribution is marginal. As monitored with the IR camera (Fig. 11c), a liquid zone appears in the condenser and gains in space as the charge is increased. Consequently, the condenser outlet subcooling rises while its inlet superheat decreases. On the other hand, the evaporator charge and operation are little impacted, as if blind to the fluid accumulation occurring in the low-pressure side of the ORC[6]. Its operation is mainly dictated by the WF and the HTF supply conditions. From a charge point of view, the evaporator operates on its own, while the liquid receiver and the condenser are the system's first and second mass dampers.

Another lesson can be learned from the above data: a poorly-selected charge significantly reduces the system performance. If the ORC is over-overcharged, the liquid receiver is completely flooded and a liquid zone appears in the condenser. The surface area available for the fluid condensation thus diminishes. The temperature difference between the air and the fluid spontaneously rises and the ORC condensing pressure is increased. As the evaporating pressure remains stable, the overall cycle pressure ratio decreases which penalizes the system performance. As shown in Fig. 11a, the ORC net efficiency drops from 6 to 2% as the system charge is risen from 20 kg to 30 kg.

4.3. Charge distribution mechanisms

The conservation of mass implies a direct dependency between the different components operation. In the present system architecture, this relationship is a "master/slave" communication from the evaporator to the liquid receiver and the condenser. As evidenced previously, the evaporator charge requirement almost solely depends on the heat source and the WF supply conditions. Consequently, the condenser and the liquid receiver are slaves as they must adapt their operating regimes so as to absorb the remaining amount of working fluid. Depending on the relative charge required by the evaporator, three scenarios can be met as depicted in Fig. 12:

(i) *Normal operation:* the charge needed by the evaporator is within design expectations. The rest of the working fluid is mainly absorbed by the liquid receiver but it remains partially filled. The presence of a two-phase equilibrium in the receiver imposes a saturated liquid fluid to leave the condenser which does not enclose any liquid zone [3]. The condensing pressure is thus minimized and the ORC performance is optimal.

(ii) *Flooded liquid receiver:* the charge in the evaporator is below design expectations. Such a scenario occurs if a too large superheating is reached at the evaporator outlet, the receiver is too small or if the charge in the ORC is too high (e.g. the operating conditions presented in Fig. 10). A lot of fluid must be spread in the low-pressure components and it cannot only be absorbed by the receiver. The tank is thus fully filled by liquid and a part of the condenser is flooded too (i.e. appearance of a liquid zone and a positive outlet subcooling). Since a smaller surface area in the condenser is available for the fluid condensation, the condensing pressure is naturally risen and the expander power output is penalized.

(iii) *Emptied liquid receiver:* the charge in the evaporator is above design expectations. This situation occurs if the fluid is not sufficiently vaporized in the evaporator or if the system charge is too low. Since most of the fluid is needed in the evaporator, the liquid receiver gets fully filled by vapour. Ultimately, the fluid density collapses in the interconnecting pipe, the net suction head seen at the pump inlet drops significantly and cavitation can be triggered. This situation is by far the most hazardous and must be avoided during the ORC operation. To this end, a minimum liquid level is generally ensured in the receiver whatever the operating conditions.

[6] The impact on the evaporator is marginal, but not absent. The rising subcooling at the condenser outlet influences the evaporator in two ways. Firstly, the fluid density at the pump inlet slightly increases which marginally raises the mass flow rate and, by extension, the evaporating pressure. Secondly, the decrease of temperature at the condenser outlet is transferred through the pump and the recuperator which, ultimately, leads to a lower temperature at the evaporator supply port. The combination of both effects tends to increase the amount of liquid in the evaporator, but on a much smaller scale than the condenser response.

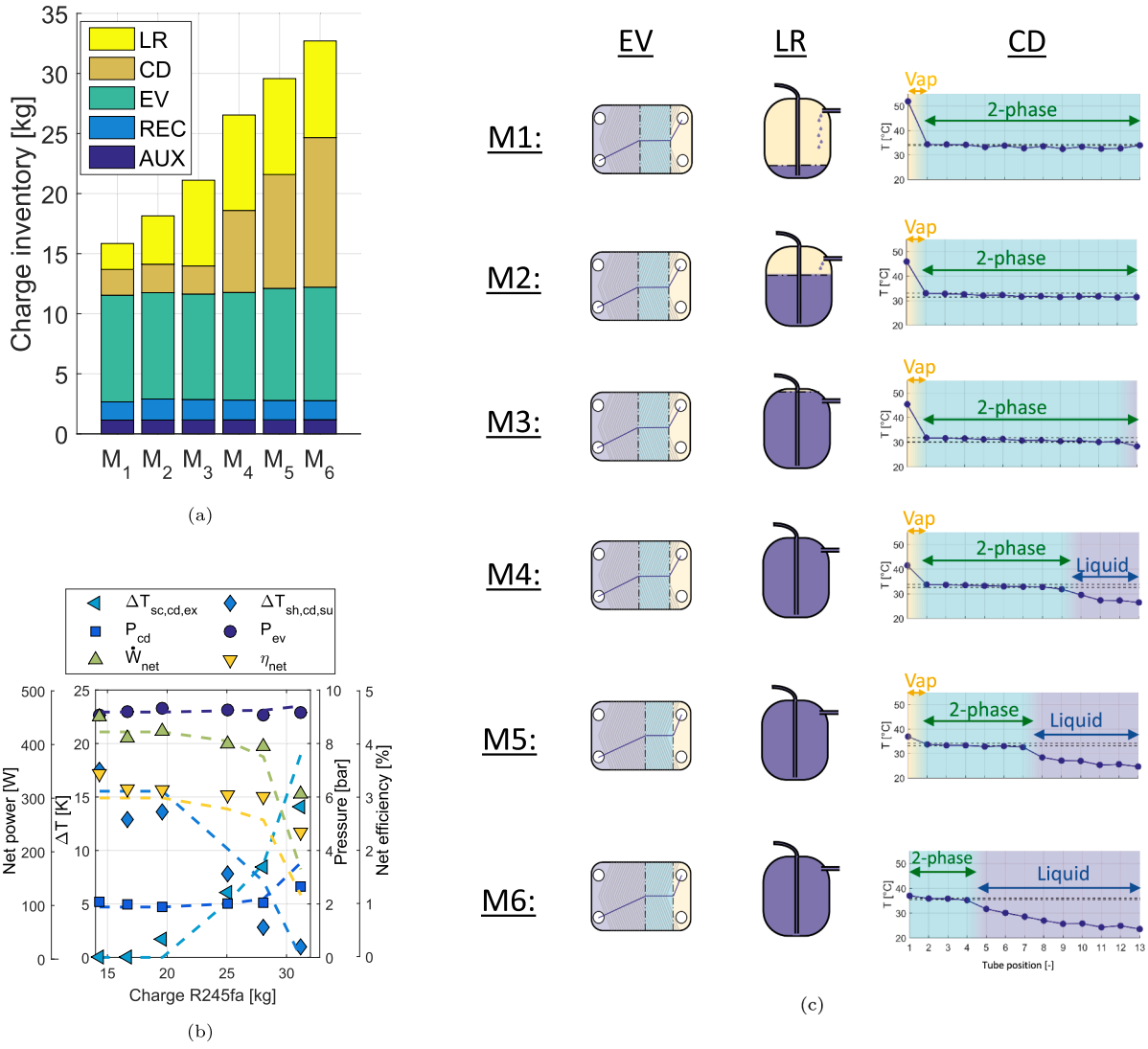

Fig. 11. Experimental measurements of six points (#15, #160, #194, #251, #301 and #325) in which the mass is increased while the other boundary conditions are kept constant. (a) Charge inventories. (b) Subcooling, superheating, pressures, power output and net conversion efficiency (dashed lines correspond to modelling predictions for which the ambient temperature is imposed at 23 °C) (c) Phases distribution.

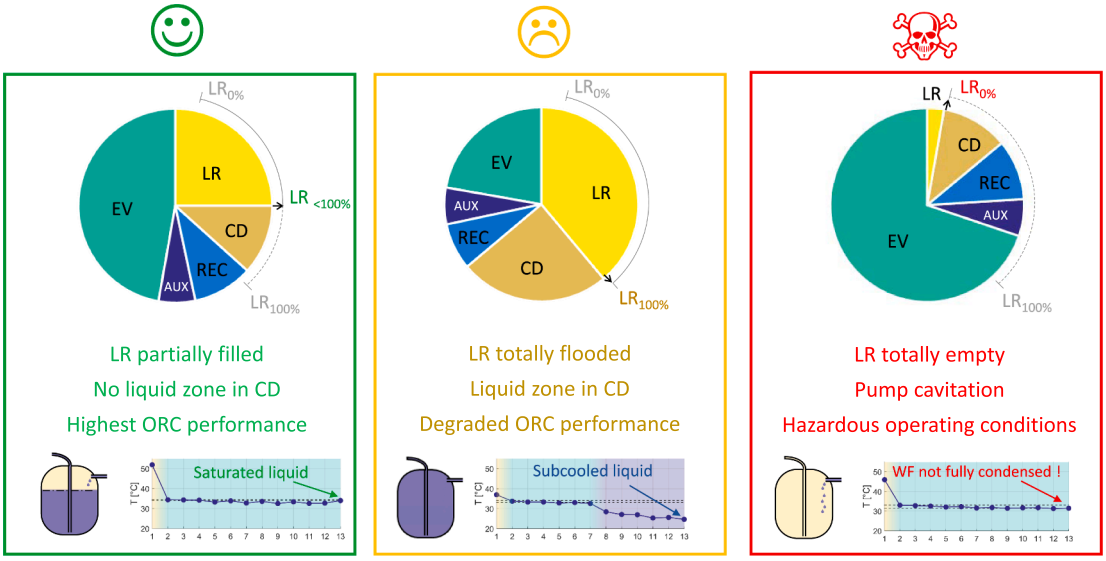

Fig. 12. Operational scenarios regarding the charge distribution (pie charts represent the relative fluid reparations among the ORC components).

In order to optimize its performance, both the fluid charge and the receiver size also appear to be important variables[7] when designing an ORC unit. Their selection must ensure that the system will remain in a normal scenario (i.e. with the liquid receiver partially filled) over its entire range of operation. To this end, a charge-sensitive model can be used as predictive design tool. For the interested reader, a method is extensively documented in Dickes's PhD thesis [25]. Using such tools, the optimal charge estimated for the present test rig appears to be 18.3 kg while the optimal reservoir size is 7.6 l.

4.4. System operation and charge distribution

The ORC operation and performance are fully determined by its boundary environment, namely the heat source/heat sink supply conditions, the machinery rotational speeds and the system charge. This section aims to emphasize the individual impact of these parameters on the ORC charge distribution. To this end, pairs of experimental points featuring the same conditions (at the exception of the variable to be investigated) are selected and compared. The impact of the system charge is already presented in Section 4.2. Similar discussions are conducted below for the other boundary inputs.

4.4.1. Impact of the heat source temperature

Fig. 13 depicts the ORC response when rising the heat source temperature and keeping all the other inputs as constant as possible. The higher the heat source temperature, the higher the fluid superheating at the evaporator outlet. The gain in fluid superheating is transferred across the expander and a larger temperature difference is seen at the recuperator supply ports. The internal heat regeneration is enhanced and a lower subcooling is reached at the evaporator inlet. The evaporator thus encloses less liquid, its charge decreases and some fluid is transferred to the low-pressure components. If the liquid receiver is partially filled (case in Fig. 13a), the charge lost by the evaporator is entirely absorbed by the reservoir and the condensing pressure remains stable. However, if the liquid receiver is completely flooded (see Fig. 13b), the charge is absorbed by the condenser - whose liquid zone is growing - and the condensing pressure increases.

4.4.2. Impact of the heat source mass flow rate

The impact of rising the heat source mass flow rate is similar as rising its supply temperature (Fig. 14). The evaporator outlet superheat increases too and the pinch point moves from the saturated liquid corner to the hot port. Following the same mechanisms, the evaporator charge decreases and some fluid is transferred to the liquid receiver (case in Fig. 14a) and/or to the condenser (case in Fig. 14b). If the condenser acts as mass damper, a liquid zone spreads inside the heat exchanger and the condensing pressure increases.

4.4.3. Impact of the heat sink mass flow rate

Fig. 15 depicts the ORC response when the air flow through the condenser is increased. The rise of air flow decreases its temperature glide in the condenser, which lowers the condensing pressure. As the condensing temperature decreases, the cycle temperatures are globally shifted downward (i.e. $T_{cd,ex}$ decreases so $T_{pp,su} \rightarrow T_{pp,ex} \rightarrow T_{recc,su} \rightarrow T_{ev,su} \rightarrow T_{exp,su} \rightarrow T_{rech,su}$ decrease too). As the evaporating pressure is marginally impacted, the evaporator becomes more filled by liquid (higher inlet subcooling, lower outlet superheating) and its charge enclosure increases. If the receiver is completely flooded (case in Fig. 15a), the charge is withdrawn from the condenser, otherwise the fluid is taken from the reservoir (case in Fig. 15b).

4.4.4. Impact of the heat sink temperature

As shown in Fig. 16, the phenomena induced by a change of the heat sink temperature are comparable to a modification of its flow rate, but inversely[8]. Given the location of the pinch point at the saturated vapour corner, the condensing pressure is lifted proportionally as the air temperature rises. As $T_{cd,ex}$ increases, the cycle temperatures are globally shifted upward all over the ORC. In response to the rise of $T_{exp,su}$, the evaporating pressure is marginally increased to stabilize the expander inlet density and to balance the flow rates delivered by the pump and swallowed by the expander ($\dot{m}_{pp}$ vs. $\dot{V}_{exp,su}$). Combining such a shift of temperatures with a little impact on the evaporating pressure, the evaporator outlet superheat (resp. inlet subcooling) increases (resp. decreases). The evaporator becomes more filled by vapour and its charge requirement diminishes. Some fluid is thus transferred to the low-pressure components: priorly to the liquid receiver (case in Fig. 16a), then to the condenser (case in Fig. 16b).

4.4.5. Impact of the pump speed

The pump speed controls the WF flow rate trough the ORC circuit. If the pump speed is increased like in Fig. 17, the WF flow rises proportionally. The volumetric flow swallowed by the expander being constant, the evaporating pressure rises to increase the fluid density and to balance $\dot{m}_{pp}$ with $\dot{V}_{exp,su}$. Additionally, the increased mass flow through the evaporator lowers the WF exhaust temperature. Combining both effects, the superheating level at the evaporator outlet port diminishes. The evaporator becomes less filled by vapour and its charge enclosure increases. If the liquid receiver is completely flooded (see Fig. 17a), the charge gained by the evaporator is first taken from the condenser whose liquid zone is reduced. If there is no liquid zone available in the condenser (see Fig. 17b), the charge absorbed by the evaporator is withdrawn from the reservoir, whose liquid level is lowered.

4.4.6. Impact of the expander speed

Fig. 18 depicts the ORC response when rising the expander speed. As the volumetric flow rate swallowed by the expander increases but the mass flow rate delivered by the pump remains unchanged, the supply density at expander inlet must be lowered. Therefore, the increase of expander speed leads to a proportional drop of the evaporating pressure. The lower saturation temperature in the evaporator increases the average temperature difference between the working fluid and the HTF. The surface area being unchanged, the heat transfer rate in the evaporator is increased and the WF outlet superheating rises. The gain in fluid superheating is transferred through the expander and a larger temperature difference is seen at the recuperator supply ports. The internal heat regeneration is enhanced and a better preheating of the working fluid is obtained at the evaporator inlet. The liquid occupation in the evaporator is thus reduced and its charge enclosure drops as the expander speed rises. Therefore, the same scenarios as above are met. As long as the receiver is partially filled (case in Fig. 18a), the charge lost by the evaporator is absorbed by the reservoir and the condensing pressure is not impacted. If the liquid receiver is entirely flooded (case in Fig. 18b), the condenser gets filled by liquid, the surface area available for the fluid condensation diminishes and the condensing pressure (marginally) rises.

4.4.7. Summary

To conclude, Table 4 summarizes how each individual input of the ORC affects the components charge enclosure. The above discussion reports the main system evolutions and simplifies them by direct causality explanations. In reality, the actual state of the ORC is found as

[7] In addition to all the other parameters to be defined in a design phase, such as the nature of the working fluid, the heat exchangers geometry, the expander size, the pipelines diameters, etc.

[8] No reliable pair of points could be found in the database to emphasize the impact of the ambient air temperature. Instead, simulation results from a validated charge-sensitive model are reported.

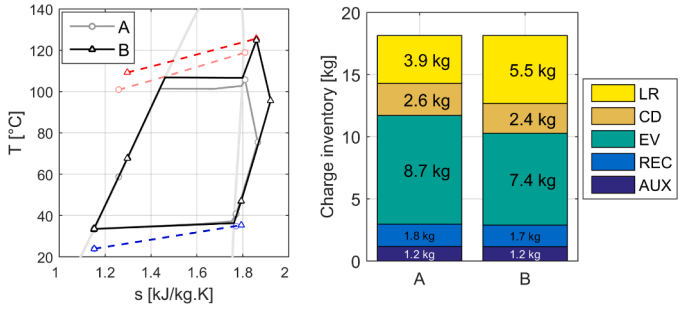

(a) Condition A: $T_{htf,h,su} = 119°C$ / Condition B: $T_{htf,h,su} = 125°C$ (points # 283 and #293 in the database).

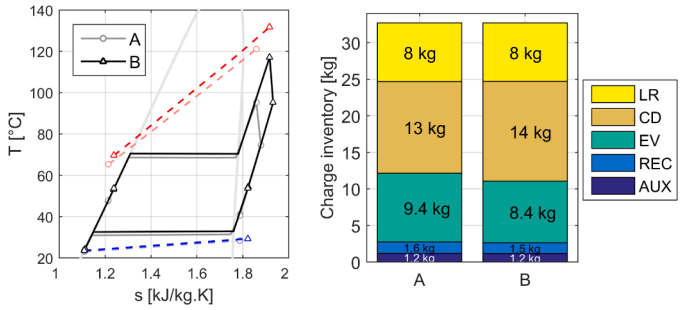

(b) Condition A: $T_{htf,h,su} = 121°C$ / Condition B: $T_{htf,h,su} = 131°C$ (points # 217 and #218 in the database).

Fig. 13. Impact of the heat source supply temperature on the system charge inventory.

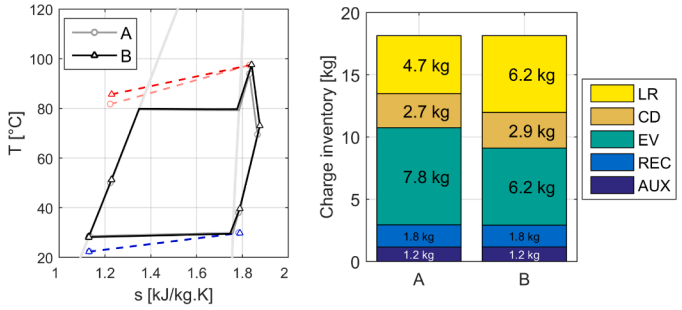

(a) Condition A: $\dot{m}_{htf,h} = 344 g/s$ / Condition B: $\dot{m}_{htf,h} = 458 g/s$ (points #264 and #263 in the database).

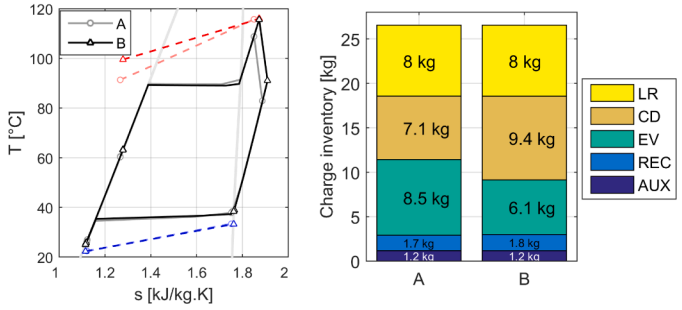

(b) Condition A: $\dot{m}_{htf,h} = 322 g/s$ / Condition B: $\dot{m}_{htf,h} = 468 g/s$ (points #66 and #65 in the database).

Fig. 14. Impact of the heat source mass flow rate on the system charge inventory.

a complex equilibrium of multiple (and sometimes, antagonist) phenomena. For a more in-depth analysis and further details regarding the ORC off-design behaviour, please refer to the full manuscript [25].

5. Conclusion

This work aims to experimentally assess how the working fluid spreads among the components of an ORC system as a function of its operating conditions. To this end, a 2-kW_e test rig is investigated as case study. Aside from standard thermo-hydraulic sensors, the test bench includes a set of bending load cells to record *on-line* the amount of fluid enclosed in the heat exchangers and the liquid receiver. Additionally, an infrared camera is used to further characterize the fluid distribution inside the condenser. Using this test bench and these means of measurement, an extensive experimental campaign is conducted. To fully characterize the ORC behaviour, all the system boundary conditions are changed, including the amount of working fluid injected in the test rig. Ultimately, a database including 330 steady-state points is collected in both full- and part-load off-design conditions. The main outcomes of this experimental work are summarized below.

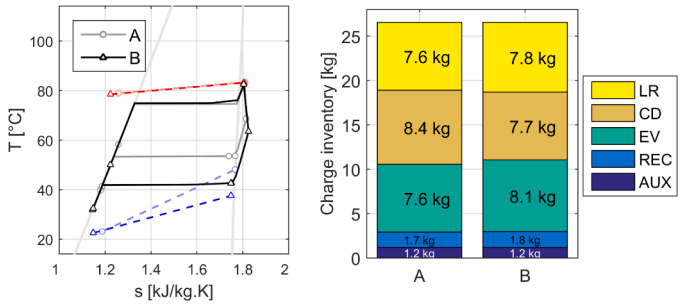

(a) Condition A: $\dot{m}_{htf,c} = 260g/s$ / Condition B: $\dot{m}_{htf,c} = 438g/s$ (points #91 and #89 in the database).

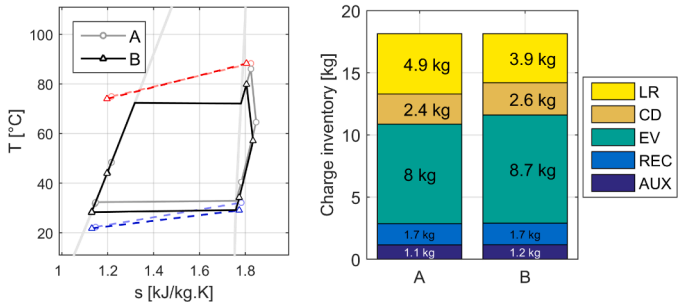

(b) Condition A: $\dot{m}_{htf,c} = 839g/s$ / Condition B: $\dot{m}_{htf,c} = 1210g/s$ (points #258 and #260 in the database).

Fig. 15. Impact of the heat sink mass flow rate on the system charge inventory.

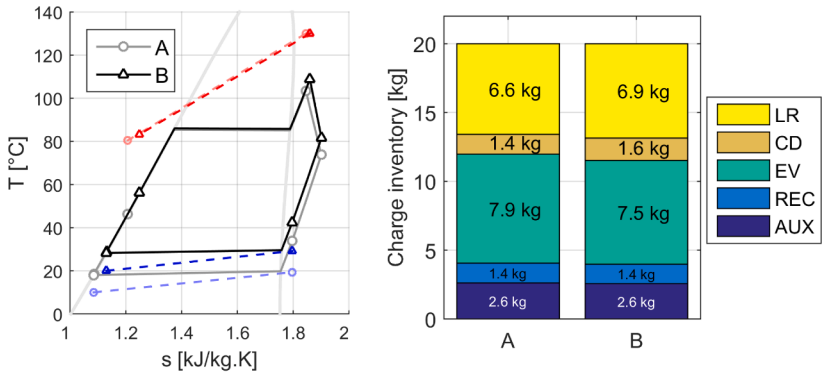

(a) Condition A: $T_{htf,c} = 10$ °C / Condition B: $T_{htf,c} = 20$ °C (simulated results).

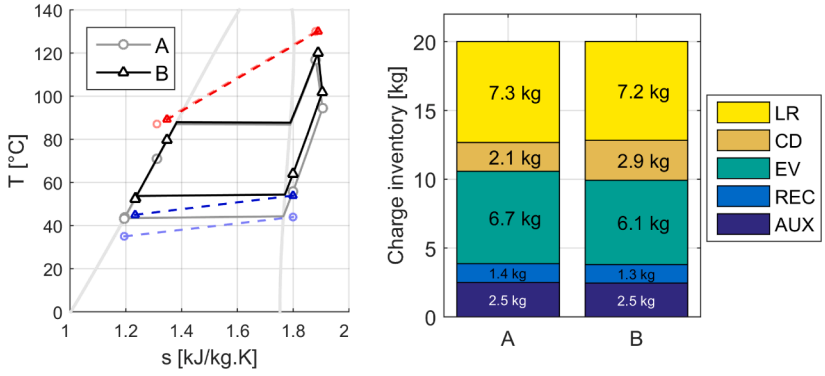

(b) Condition A: $T_{htf,c} = 35$ °C / Condition B: $T_{htf,c} = 45$ °C (simulated results).

Fig. 16. Impact of the heat sink supply temperature on the system charge inventory.

Learnings about the measurement aspects:

- The proposed on-line charge measurement technique shows both pros and cons in comparison to more traditional "quick-closing-valve" approaches. On the plus side, it permits recording of the fluid distribution without being intrusive (gain in time) and even monitoring of fluid transfers in transient regimes (e.g. in Fig. 19). On the negative side, such an approach requires a dedicated (and rather tedious) calibration of each load cell. Additionally, it results in a relatively poor accuracy as the whole components are hung to the

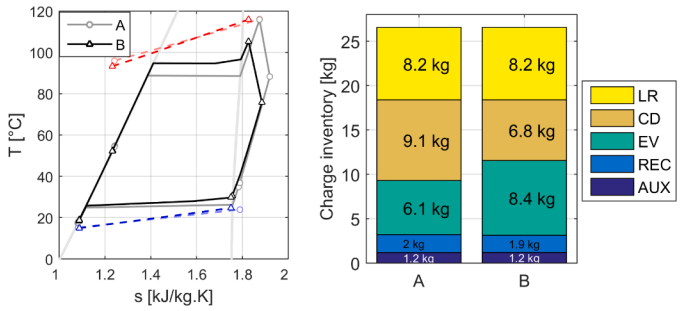

(a) Condition A: $N_{pp} = 400\ rpm$ / Condition B: $N_{pp} = 480\ rpm$ (points #95 and #97 in the database).

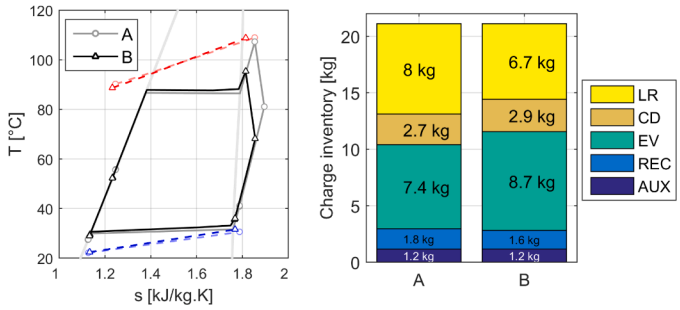

(b) Condition A: $N_{pp} = 400\ rpm$ / Condition B: $N_{pp} = 440\ rpm$ (points #225 and #228 in the database).

Fig. 17. Impact of the pump speed on the system charge inventory.

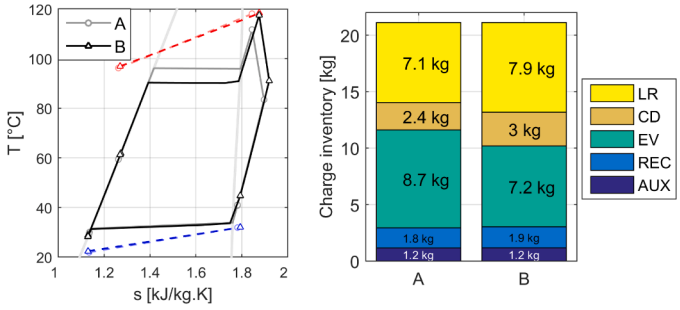

(a) Condition A: $N_{exp} = 3674\ rpm$ / Condition B: $N_{exp} = 4674\ rpm$ (points #230 and #229 in the database).

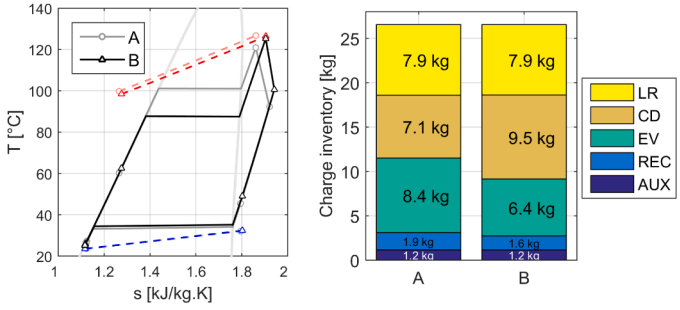

(b) Condition A: $N_{exp} = 2434\ rpm$ / Condition B: $N_{exp} = 4478\ rpm$ (points #17 and #14 in the database).

Fig. 18. Impact of the expander speed on the system charge inventory.

load cells and large-scale force transducers (up to 250 kg) are needed to detect a small amount of fluid. To refine the measurements accuracy, raw data are post-treated with a dual data reconciliation method.

- The temperature profiles gathered with the infrared camera constitute very valuable data to characterize the condenser operation. If properly post-treated, these IR photos allow to directly observe the fluid repartition within the tubes and to quantify how much of the condenser is flooded by liquid. This information corroborates the load cell measurements and visually illustrates the fluid transfers occurring in this key component.

Learnings about the charge distribution aspects:

- The charge inventory in an ORC is solely dictated by two parameters: the inner volume of the components and the fluid mean

Table 4
Influence of the ORC boundary conditions on the components charge enclosure (↗ = charge increased, ↘ = charge decreased, ≈ = charge stable). Auxiliaries include all the pipelines, the pump and the expander.

Parameter	Evaporator	Condenser	Liquid receiver	Recuperator	Aux.
Increase of heat source temperature	↘	↗	↗	≈	≈
Increase of heat source mass flow	↘	↗	↗	≈	≈
Increase of heat sink temperature	↘	↗	↗	≈	≈
Increase of heat sink mass flow	↗	↘	↘	≈	≈
Increase of pump speed	↗	↘	↘	≈	≈
Increase of expander speed	↘	↗	↗	≈	≈
Increase of system charge	≈	↗	↗	≈	≈

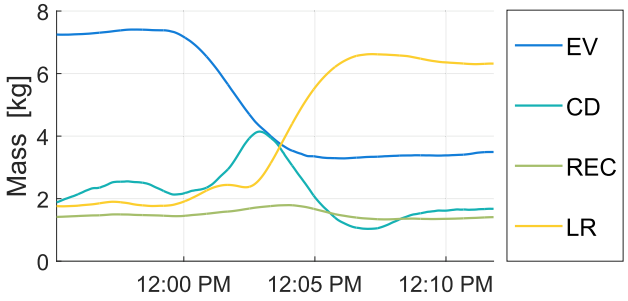

Fig. 19. Example of charge transfer in transient conditions (resulting from a simultaneous decrease of the pump and condenser fan speeds).

density within them. More specifically, the fluid distribution is mainly correlated with the spatial occupation of the liquid and the vapour phases through the system. Similarly as the charge in the receiver is given by its liquid level, there is a strong dependency between the fluid mass distribution and the temperature profiles in the heat exchangers. Besides the superheating and subcooling levels observed at their inlet and outlet ports, the amplitude and the location of the pinch point found in the heat exchangers also play an important role in their charge enclosure. Ultimately, any external parameter that impacts the heat exchangers operation and their temperature profiles will also modify the system charge distribution.

- The mass balance in such a closed-loop ORC system implies a direct dependency between the different components operation. In the present architecture (i.e. featuring an in-line liquid receiver at the condenser outlet), this is a master/slave relationship from the evaporator to the low-pressure components. The evaporator dictates its charge requirement based on its boundary conditions only while the liquid receiver and the condenser adapt their operation to absorb the remaining amount of working fluid.
- A proper selection of both the system charge and the liquid receiver size is crucial to maximize the ORC performance over its entire range of operation. If the system charge is too high (or the liquid receiver is too small), a part of the condenser may be flooded by liquid, leading to a rise in the condensing pressure and a decrease in the ORC performance. On the other hand, if the system charge is too low, cavitation may be triggered as the relative charge requirement of the evaporator becomes too high and the receiver gets entirely empty of its liquid. Optimally, the amount of fluid to inject in the ORC and the volume of the receiver must be chosen to ensure the liquid receiver to be partially filled in all cases. For the present system, an optimal charge of 18.3 kg and a receiver volume of 7.6 l are estimated with a validated charge-sensitive model.

This study constitutes a first attempt to record intrinsically the fluid distribution in an ORC unit. Besides providing original information on the system off-design behaviour, these measurements provide key information to calibrate and validate charge-sensitive modelling tools. For the sake of clarity and conciseness, this paper limited the discussion to charge-related aspects and only presented a few points from the database. For the complete story (including the simulation work, a deeper analysis of the entire database, a study of the impact of the lubricant, etc.), please refer to Dickes's PhD manuscript [25].

To conclude, it is important to note that this paper considers a single test-rig and a specific system architecture. Future works should extend such investigations to other ORC configurations and components technologies (including shell-and-tube HEXs, off-line liquid receivers, turbo-expanders, etc.) which may demonstrate different charge distribution mechanisms. Finally, this work focuses on steady-state operation only. However, a key benefit of the proposed charge measurement technique is its ability to record dynamic charge transfers in transient operations (see an example in Fig. 19). Prospective works should exploit such data to further validate dynamic off-design models of ORC systems.

Declaration of Competing Interest

The authors declare that they have no known competing financial interests or personal relationships that could have appeared to influence the work reported in this paper.

Acknowledgements

R. Dickes thanks the Fund for Scientific Research of Belgium (F.R.S - F.N.R.S) for its financial support (research fellowship FC2349).

Appendix A. Test rig details

A photo of the test rig is given in Fig. A.20 while the mechanical apparatus built to monitor the condenser, the evaporator and the liquid receiver are shown in Fig. A.21. Main properties of the components and the sensors[9] are summarized in Tables A.5 and A.6, respectively.

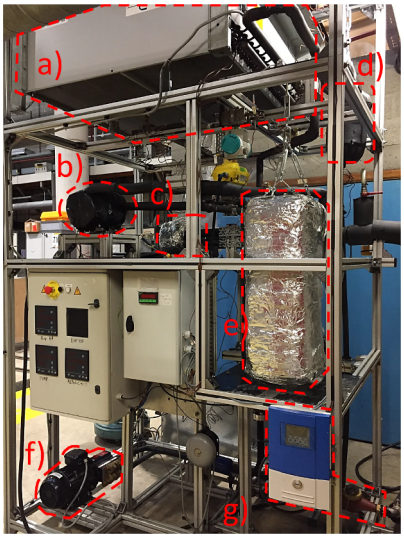

Fig. A.20. Photo of the test rig. (a) Condenser (b) Expander (c) Recuperator (d) Liquid receiver (e) Evaporator (f) Pump (g) HTF flow meters.

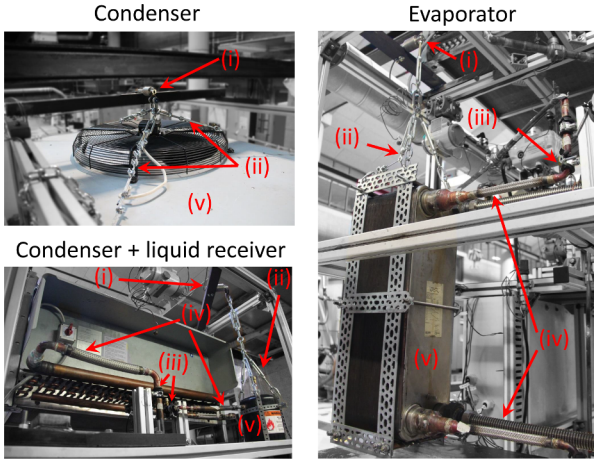

Fig. A.21. Mechanical apparatus for on-line charge measurements (i) load cell (ii) hanging structure (iii) holding clamps (iv) flexible hoses (v) component.

Table A.5
Main components and fluids of the ORC test rig.

Component	Type	Model/Brand	Comment
Working fluid	HFC	R245fa	Variable charge (14–31 kg)
Lubricant	POE oil	Emkarate RL32-3MAF	Constant charge (1.5 kg)
Heat source fluid	Thermal oil	Pirobloc HTF-Basic	Heated by boiler
Heat sink fluid	Ambient air	n.a.	n.a.
Expander	Scroll	Valeo	Variable speed (var. Ω)
Pump	Diaphragm	Hydracell G03	Variable speed (VFD)
Condenser	FCHEX	Alfa Laval Solar Junior 121	Variable speed (VFD)
Evaporator	BPHEX	Alfa Laval CB76-100E	Thermally insulated
Recuperator	BPHEX	Alfa Laval CB30-40H-F	Thermally insulated
Liquid receiver	Vertical tank	Denaline	Volume = 5.7 l

Table A.6
Details of the acquisition system and the sensors (FS = full-scale).

Variables	Sensor details	Final accuracy
Temperatures	T-type thermocouple	±0.75°C
Pressures	Piezoresistive sensors (21Y Keller)	±1.5% FS
WF mass flow rate	Optimass 7300C Coriolis flowmeter	±0.5% meas.
HTF volume flow rate	MTWH multijet flow meter	±5% meas.
Expander power	PQ-Box 100 wattmeter	±0.5% meas.
Pump power	A2000 Gossen wattmeter	±0.5% FS
Fan power	A2000 Gossen wattmeter	±0.5% FS
Evaporator mass	250 kg Tedea Huntleigh load cell	±0.75 kg[a]
Recuperator mass	50 kg Tedea Huntleigh load cell	±0.3 kg[a]
Liquid receiver mass	50 kg Tedea Huntleigh load cell	±0.1 kg[a]
Condenser mass	250 kg Tedea Huntleigh load cell	±1 kg[a]

[a] Final accuracies of the charge measurements account for the error propagation of all the sensors employed in the mass monitoring (i.e. the load cells, but also the temperature and the pressure transducers, cfr. Eq. (1)).

Appendix B. Experimental database

All the experimental data presented in this work are available in Dickes's PhD appendix [25], freely accessible at https://orbi.uliege.be/handle/2268/233945. The database includes more 330 steady-state points and covers wide ranges of conditions as depicted in Fig. B.22. All measurements (raw and reconciled) are reported in a spreadsheet (ExperimentalData_spreadsheet.xlsx) and in a ID document describing every point individually (ExperimentalData_reports.pdf). An example of ID card is given in Fig. B.23 for one point. Finally, constraint equations employed for the dual data reconciliation are reported in Eqs. (B.1)-(B.14).

$$\dot{Q}_{wf,ev} = \dot{Q}_{htf,h,ev} \tag{B.1}$$

$$\dot{Q}_{wf,cd} = \dot{Q}_{htf,c,cd} \tag{B.2}$$

$$\dot{Q}_{wf,h,rec} = \dot{Q}_{wf,c,rec} \tag{B.3}$$

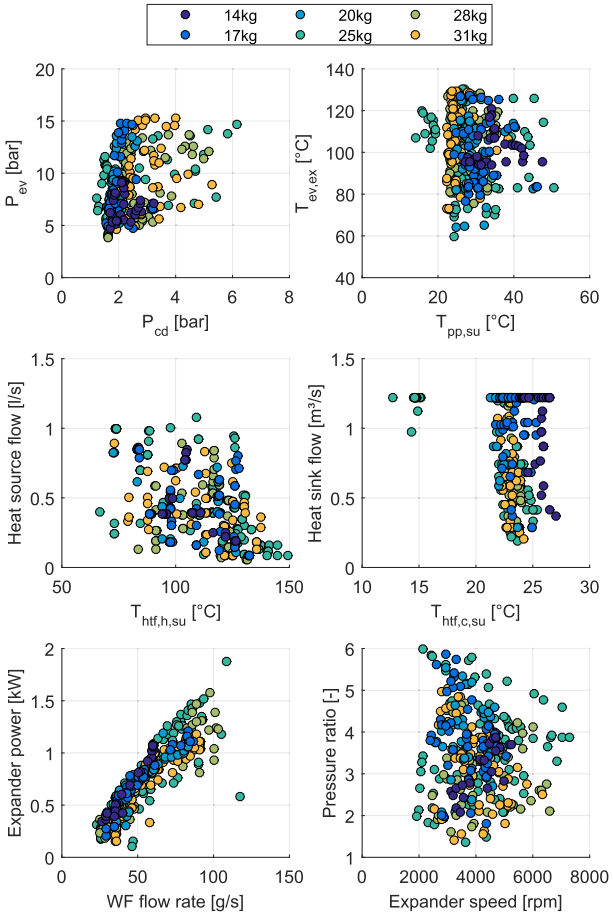

Fig. B.22. Operating conditions covered by the experimental campaign (colors of the markers differentiate the different charges tested in the ORC system).

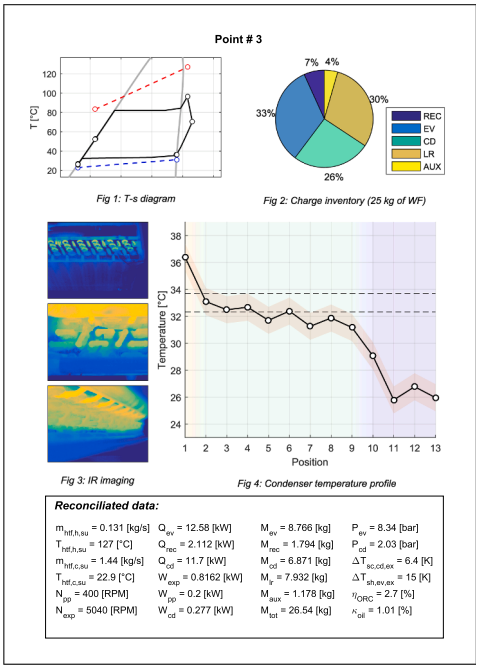

Fig. B.23. Example of ID card for one operating point (point #3).

$$P_{exp,su} = P_{exp,ex} + \Delta P_{exp} \tag{B.4}$$

$$P_{ev,su} = P_{ev,ex} + \Delta P_{ev} \tag{B.5}$$

$$P_{cd,su} = P_{cd,ex} + \Delta P_{cd} \tag{B.6}$$

$$P_{pp,su} = P_{cd,ex} + \rho_{cd,ex} g H_{pp} \tag{B.7}$$

$$x_{cd,ex} = 0 \text{ if } L_{LR} \in [0, 1] \tag{B.8}$$

$$P_{pp,ex} > P_{ev,su} \tag{B.9}$$

$$P_{exp,ex} > P_{cd,su} \tag{B.10}$$

$$\theta_{ev} \geqslant 0 \tag{B.11}$$

$$\theta_{cd} \geqslant 0 \tag{B.12}$$

$$\theta_{rec} \geqslant 0 \tag{B.13}$$

$$M_{tot} = M_{lc,ev} + M_{lc,cd} + M_{lc,rec} + M_{lc,lr} + \sum_{j} M_{others,j} \tag{B.14}$$

Appendix C. Supplementary material

Supplementary data associated with this article can be found, in the online version, at https://doi.org/10.1016/j.applthermaleng.2020.115689.

References

[1] E. Macchi, M. Astolfi, Organic Rankine Cycle (ORC) Power Systems - Technologies and Applications, elsvier ed., Woodhead Publishing Series in Energy, 2016.
[2] R. Dickes, O. Dumont, R. Daccord, S. Quoilin, V. Lemort, Modelling of organic Rankine cycle power systems in off-design conditions: an experimentally-validated comparative study, Energy 123 (2017) 710–727, https://doi.org/10.1016/j.energy.2017.01.130 URL http://hdl.handle.net/2268/207441.
[3] R. Dickes, O. Dumont, S. Quoilin, V. Lemort, Charge-sensitive modelling of organic Rankine cycle power systems for off-design performance simulation, Appl. Energy 212 (2018) 1262–1281, https://doi.org/10.1016/j.apenergy.2018.01.004.
[4] M. Yousefzadeh, E. Uzgoren, Mass-conserving dynamic organic Rankine cycle model to investigate the link between mass distribution and system state, Energy 93 (2015) 1128–1139, https://doi.org/10.1016/j.energy.2015.09.102.
[5] A. Desideri, Dynamic Modeling of Organic Rankine Cycle Power Systems, Phd thesis University of Liège, 2016.
[6] D. Ziviani, B. Woodland, E. Georges, E. Groll, J. Braun, W. Horton, M. van den Broek, M. De Paepe, Development and a Validation of a Charge Sensitive Organic Rankine Cycle (ORC) Simulation Tool, Energies 9 (6) (2016) 389, https://doi.org/10.3390/en9060389 URL http://www.mdpi.com/1996-1073/9/6/389.
[7] L. Liu, T. Zhu, J. Ma, Working fluid charge oriented off-design modeling of a small scale Organic Rankine Cycle system, Energy Convers. Manage. 148 (2017) 944–953, https://doi.org/10.1016/j.enconman.2017.06.009.
[8] M. Santos, J. André, S. Francisco, R. Mendes, J. Ribeiro, Off-design modelling of an organic Rankine cycle micro-CHP: Modular framework, calibration and validation, Appl. Therm. Eng. 137 (March) (2018) 848–867, https://doi.org/10.1016/j.applthermaleng.2018.04.009.
[9] Y. Pan, L. Liu, T. Zhu, Simulation of working fluid mass distribution in small-scale Organic Rankine Cycle system under sub-critical conditions, Appl. Therm. Eng. 131 (2018) 884–896, https://doi.org/10.1016/j.applthermaleng.2017.12.017.
[10] N. Tanaka, M. Ikeuchi, G. Yamanaka, Experimental study on the dynamic characteristics of a heat pump, ASHRAE Trans. (1982).
[11] W. Mulroy, D. Didion, A laboratory investigation of refrigerant migration in a split unit air conditioner, Tech. rep., U.S Department of Commerce, 1983.
[12] W. Miller, The laboratory evaluation of the heating mode part-load operation of an air-to-air heat pump, ASHRAE Trans. (1985).
[13] M.I. Belth, T.E. Grzymala, D.R. Tree, Transient mass flow rate of a residential air-to-

air heat pump, Int. J. Refrig. 11 (5) (1988) 298–304, https://doi.org/10.1016/0140-7007(88)90092-8.
[14] M. Grodent, Contribution à l'étude des composants de systèmes frigorifiques: modélisation en régime stationnaire et validation expérimentale. Application des modèles développés à l'étude d'un système bisplit, Ph.D. thesis University à Liège, 1998.
[15] F.W. Primal, S. Oxana, L. Per, B. Palm, Charge Distribution in a 5kW Heat Pump Using Propane as Working Fluid: Part 1: Experimental Investigation, in: 16. Nordiske Kølemøde og 9. Nordiske Varmepumpedage, 2001, p. 299.
[16] M.R. Hoehne, P.S. Hrnjak, Charge Minimization in Systems and Components Using Hydrocarbons as a Refrigerant, Tech. rep., ACRC - University of Illinois, Urbana-Champaign, IL, 2004. URL https://www.ideals.illinois.edu/handle/2142/12315.
[17] E. Björk, B. Palm, Refrigerant mass charge distribution in a domestic refrigerator, Part I: Transient conditions, Appl. Therm. Eng. 26 (2006) 829–837, https://doi.org/10.1016/j.applthermaleng.2005.10.003.
[18] E. Björk, B. Palm, Refrigerant mass charge distribution in a domestic refrigerator, Part II: Steady state conditions, Appl. Therm. Eng. 26 (2006) 866–871, https://doi.org/10.1016/j.applthermaleng.2005.10.003.
[19] G. Ding, X. Ma, P. Zhang, W. Han, S. Kasahara, T. Yamaguchi, Practical methods for measuring refrigerant mass distribution inside refrigeration system, Int. J. Refrig. 32 (2009) 327–334, https://doi.org/10.1016/j.ijrefrig.2008.05.002.
[20] S. Peuker, Experimental and analytical investigation of refrigerant and lubricant migration, Phd thesis University of Illinois at Urbana-Champaign, 2010.
[21] S.S. Wujek, C.D. Bowers, J.W. Powell, R.A. Urrego, E.T. Hessell, T.L. Benanti, Refrigerant and lubricant mass distribution in a convertible split system residential air-conditioner, in: Proceedings of Purdue 2014, Purdue (USA), 2014, pp. 1–10.
[22] T. Li, J. Lu, L. Chen, D. He, X. Qiu, H. Li, Z. Liu, Measurement of refrigerant mass distribution within a R290 split air conditioner, Int. J. Refrig. 57 (2015) 163–172, https://doi.org/10.1016/j.ijrefrig.2015.05.012.
[23] W. Tang, G. He, D. Cai, Y. Zhu, A. Zhang, Q. Tian, The experimental investigation of refrigerant distribution and leaking characteristics of R290 in split type household air conditioner, Appl. Therm. Eng. 115 (2017) 72–80, https://doi.org/10.1016/j.applthermaleng.2016.12.083.
[24] J. Li, W. Deng, G. Yan, Improving quick cooling performance of a R410A split air conditioner during startup by actively controlling refrigerant mass migration, Appl. Therm. Eng. 128 (2018) 141–150, https://doi.org/10.1016/j.applthermaleng.2017.08.151.
[25] R. Dickes, Charge-sensitive methods for the off-design performance characterization of organic Rankine cycle (ORC) power systems, Phd thesis University of Liège, 2019.
[26] E. Georges, S. Declaye, O. Dumont, S. Quoilin, V. Lemort, Design of a small-scale organic Rankine cycle engine used in a solar power plant, Int. J. Low-Carbon Technol. 8 (2013) 34–41, https://doi.org/10.1093/ijlct/ctt030 URL http://hdl.handle.net/2268/149519.
[27] R. Dickes, O. Dumont, S. Declaye, S. Quoilin, I. Bell, V. Lemort, Experimental investigation of an ORC system for a micro-solar power plant, Proceedings of the 22nd International Compressor Engineering at Purdue, Purdue (USA), 2014 URL http://hdl.handle.net/2268/170508.
[28] A. Bryszewska-Mazurek, T. Świeboda, W. Mazurek, Performance analysis of a solar-powered organic rankine cycle engine, J. Air & Waste Manage. Assoc. 61 (1) (2011) 3–6, https://doi.org/10.3155/1047-3289.61.1.3.
[29] S. Baral, D. Kim, E. Yun, K. Kim, Experimental and Thermoeconomic Analysis of Small-Scale Solar Organic Rankine Cycle (SORC) System, Entropy 17 (2015) 2039–2061, https://doi.org/10.3390/e17042039 URL http://www.mdpi.com/1099-4300/17/4/2039/.
[30] M. Orosz, A. Mueller, S. Quoilin, H. Hemond, Small scale solar orc system for distributed power in Lesotho, in: 29th ISES Biennial Solar World Congress 2009, ISES 2009, Vol. 2, 2009, pp. 1042–1048. http://www.scopus.com/inward/record.url?eid=2-s2.0-84873835908&partnerID=tZOtx3y1.
[31] Electratherm, Product catalogue: Power+ Generator. URL www.electratherm.com.
[32] Rank, Product catalogue: LT/MT/HT/HTC units. URL www.rank-orc.com.
[33] R. Dickes, O. Dumont, V. Lemort, Infrared imaging of a multi-zone condenser for heat transfer coefficients assessment, in: Proceedings of ECOS 2019, Worclaw (Poland), 2019, pp. 1–12.
[34] G.M. Carlomagno, G. Cardone, Infrared thermography for convective heat transfer measurements, Exp. Fluids 49 (6) (2010) 1187–1218, https://doi.org/10.1007/s00348-010-0912-2.
[35] G.A. Longo, S. Mancin, G. Righetti, C. Zilio, HFC32 vaporisation inside a Brazed Plate Heat Exchanger (BPHE): Experimental measurements and IR thermography analysis, Int. J. Refrig. 57 (2015) 77–86, https://doi.org/10.1016/j.ijrefrig.2015.04.017.
[36] G.A. Longo, Vaporisation of the low GWP refrigerant HFO1234yf inside a brazed plate heat exchanger, Int. J. Refrig. 35 (4) (2012) 952–961, https://doi.org/10.1016/j.ijrefrig.2011.12.012.